DOI: 10.24874/ti.2168.03.26.06

Tribology in Industry

www.tribology.rs

RESEARCH

Response Surface Modelling of Friction and Wear Behaviour of Nano-Enhanced Peltophorum Pterocarpum Biodiesel under Boundary Lubrication

T. Dayananda Murthy[a,*], H. Yogish[a], N.S. Kumaraswamy [a], R. Pavankumar [a]

[a]*Department of Mechanical Engineering, SJCE, JSS Science and Technology University, Mysore, India.*

Keywords:

Biodiesel
MoS_2 Nano-additive
Boundary lubrication
Response surface methodology
coefficient of friction
wear rate

* Corresponding author:

Dayananda Murthy T
E-mail:
dayanandamurthy21@gmail.com

Received: 30 March 2026
Revised: 6 May 2026
Accepted: 19 May 2026

A B S T R A C T

This work investigates the boundary lubrication behaviour of Peltophorum pterocarpum biodiesel enhanced with MoS_2 nanoparticles through statistically planned pin-on-disc experiments and response surface modelling. The biodiesel satisfied the principal ASTM D6751 and EN 14214 property limits considered in this study. MoS_2 nanoparticles with platelet/nanosheet morphology and 70-90 nm average particle size were dispersed at 0-150 ppm, while normal load and sliding speed were varied within 10-40 N and 0.25-1.00 m/s, respectively. A Box-Behnken design was used to model coefficient of friction (COF), wear rate, and post-test surface roughness for AISI 52100 steel contacts. COF and wear rate ranged from 0.094-0.132 and 2.30-4.20 x 10^{-6} $mm^3/N{\cdot}m$, respectively. ANOVA showed significant quadratic models for COF (R^2 = 0.945) and wear rate (R^2 = 0.902), with nano-additive concentration, load, and speed being the dominant factors. Confirmation testing at 135 ppm MoS_2, 12 N, and 1.00 m/s yielded 0.093 ± 0.002 COF, 2.34 ± 0.09 x 10^{-6} $mm^3/N{\cdot}m$ wear rate, and 0.26 ± 0.01 µm roughness, corresponding to 3.33-4.00% absolute prediction errors. XRD and EDS results indicate a thin MoS_2-/oxide-/carbon-containing tribofilm, supporting a lubrication mechanism involving reduced metal-to-metal contact, lower shear at the interface, and partial filling or smoothing of surface asperities.

1. INTRODUCTION

The reduction of friction and wear in fuel-lubricated steel contacts is essential for improving the durability and efficiency of components operating under boundary lubrication. Screening of vegetable-oil alcohol esters established their usefulness as fuel-lubricity enhancers [1]. Work on specific fatty acid methyl esters demonstrated that diesel-fuel lubricity depends on individual ester species and molecular structure [2]. The origin of biodiesel lubricity has been linked to polar ester structures and oxygenated components that can adsorb on metallic surfaces [3]. Studies of hydroxylated methyl esters further showed

that these compounds can improve diesel-fuel lubricity [4]. Biodiesel addition has also been shown to enhance the lubricity of low-sulphur diesel fuels [5].

Biodiesel performance nevertheless depends on feedstock chemistry, FAME composition and fuel stability. A review of biodiesel tribology linked performance to stability and physicochemical properties [6]. Studies on vegetable-oil and duck-fat-derived biodiesels showed that FAME composition influences tribological behaviour [7]. Palm biodiesel, petroleum-diesel and hydrogenated-vegetable-oil blends have also shown composition-dependent lubricity [8]. Comparative work on desert-seed-oil-derived biodiesel and bio-lubricant systems indicated that renewable feedstock selection affects lubrication performance [9]. A recent review of bio-additives in diesel fuels further confirmed that additive formulation remains an important route for improving tribological behaviour [10]. In this study, Peltophorum pterocarpum biodiesel was selected because it is a renewable, non-edible feedstock and because the optimized fuel satisfied the principal ASTM D6751 and EN 14214 property limits evaluated in this work.

Nano-additive technology offers a practical route for improving the friction-reducing and wear-resistant behaviour of renewable base fluids. Additivized biodiesel blends have been shown to modify engine performance, emissions and lubricity [11]. Palm-sesame biodiesel fuels containing alcoholic and nanoparticle additives produced measurable changes in lubricating-oil tribological response during four-ball testing [12]. Nanoparticle additives have also been demonstrated to alter the lubricity of diesel and biodiesel fuels [13]. For MoS_2-based additives, a recent review described the low-shear layered structure and tribofilm-related lubrication behaviour of MoS_2 nanomaterials [14]. Experimental measurements of ZnO and MoS_2 diesel-oil nanofluids showed that viscosity, physicochemical behaviour and tribological performance are closely linked [15]. Fe_3O_4/MoS_2 nanocomposite additives have been examined in aqueous and oil media [16], and magnetic MoS_2 composites have been reported to provide a repair effect under soot-induced wear [17]. MoS_2 can also act synergistically with graphene nanohybrids in diesel-based engine oil [18], whereas antagonism between nano-MoS_2 and soot particles has been reported in ester base oil [19]. These contrasting observations show that additive concentration, dispersion stability and operating severity must be optimized rather than assumed to be universally beneficial.

The friction and wear mechanisms in biodiesel-based boundary lubrication are expected to involve more than one effect. Research on unsaturated fatty acids in diesel fuels attributed friction reduction to surface interactions of fatty-acid species [20]. Tribochemical studies of unsaturated fatty acids used as friction modifiers in (bio)diesel fuels identified surface reactions that can influence boundary-film formation [21]. Work on ZDDP and methyl oleate in biodiesel-fuelled engine contexts reported synergistic nano-tribological interactions [22]. These findings imply that Peltophorum biodiesel and MoS_2 may act through simultaneous adsorption, tribochemical reaction, particle shearing and composite-film formation. This interpretation is also consistent with the green-tribology framework in which renewable lubricants are improved by reducing energy loss and wear [23]. Response surface methodology (RSM) is suitable for this problem because friction and wear are influenced by simultaneous linear, quadratic and interaction effects. The Box-Behnken design provides an efficient three-level experimental design for studying quantitative variables without requiring a full factorial matrix [24]. Standard design-of-experiments guidance explains how quadratic response-surface models and confirmation tests can be used to evaluate curvature, interactions and model adequacy in engineering experiments [25].

The original contribution of the present study is therefore threefold. First, it develops a Box-Behnken RSM model for nano-enhanced Peltophorum pterocarpum biodiesel under boundary-lubricated steel contact, a system for which combined optimization data are limited. Second, it evaluates COF, wear rate, and surface roughness together rather than treating friction alone as the performance indicator. Third, it connects the statistical trends with surface evidence from XRD and EDS, thereby linking the regression coefficients and factor interactions to plausible tribofilm and asperity contact mechanisms.

2. MATERIALS AND METHODS

2.1 Biodiesel and nano-additive preparation

Peltophorum pterocarpum oil was filtered and pre-treated prior to transesterification, and the resulting B100 biodiesel was evaluated in terms of density, kinematic viscosity, acid value, flash point, water content, oxidation stability, FAME content, and calorific value. As summarized in Table 1, the optimized fuel met the principal specification limits used in this study, supporting its use as a stable base fluid for tribological evaluation.

Table 1. Physicochemical properties of optimized Peltophorum pterocarpum biodiesel.

Property	Unit	Value	Standard / specification
Density at 15 °C	kg/m^3	882	EN 14214: 860–900
Kinematic viscosity at 40 °C	mm^2/s	4.62	ASTM D6751: 1.9–6.0; EN 14214: 3.5–5.0
Acid value	mg KOH/g	0.34	ASTM D6751 / EN 14214: ≤ 0.50
Flash point	°C	168	ASTM D6751: ≥ 93
Water content	mg/kg	310	EN 14214: ≤ 500
Oxidation stability	h	6.4	EN 14214: ≥ 6
FAME content	wt.%	97.3	EN 14214: ≥ 96.5
Calorific value	MJ/kg	39.8	No fixed limit

The nano-additive used in the present study was molybdenum disulfide (MoS_2) nanopowder with an average particle size of 70-90 nm, a purity of not less than 99%, and a platelet/nanosheet-like morphology, as summarized in Table 2. The nanopowder appeared dark grey to black in colour and was used as received for the preparation of nano-enhanced biodiesel samples. The morphology is discussed using FESEM micrographs in Section 3.5.

Table 2. Properties of the MoS_2 nano-additive used in the present study.

Parameter	Value
Nano-additive	Molybdenum disulfide (MoS_2) nanopowder
Average particle size	70–90 nm
Purity	≥ 99%
Morphology	Platelet / nanosheet-like
Specific surface area	40 ± 5 m^2/g
Density	5.06 g/cm^3
Appearance	Dark grey to black powder
Working concentration range in biodiesel	0–150 ppm

2.2 Tribological testing and design of experiments

Figure 1 shows the pin-on-disc tribometer, and Figure 2 summarizes the experimental workflow. After nanoparticle dispersion into biodiesel by ultrasonication, tribological measurements were performed under lubricated boundary conditions according to ASTM G99 using AISI 52100 steel specimens. The selected operating ranges were 0-150 ppm nano-additive concentration, 10-40 N normal load, and 0.25-1.00 m/s sliding speed, with a sliding duration of 300 s. The tests were not dry-sliding experiments; biodiesel or MoS_2 nano-enhanced biodiesel was supplied at the contact interface. The ambient test conditions were 27 ± 2 °C and 55 ± 5% relative humidity. These factor levels define the coded design space shown in Table 3.

Fig. 1. Pin-on-disc tribometer employed for friction and wear experiments.

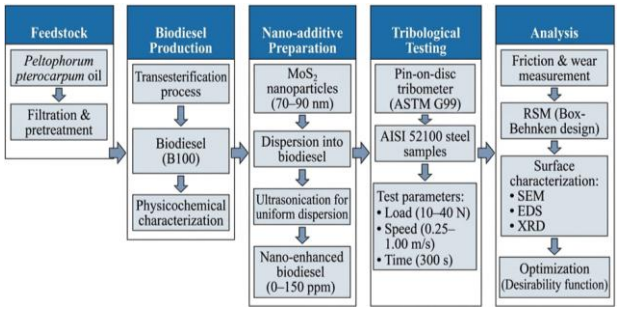

Fig. 2. Schematic representation of the experimental methodology.

Table 3. Box-Behnken design factors and levels

Factor	Symbol	Unit	-1	0	+1
Nano-additive concentration	X_1	ppm	0	75	150
Normal load	X_2	N	10	25	40
Sliding speed	X_3	m/s	0.25	0.625	1.00

For the preparation of nano-enhanced biodiesel, the required mass of MoS_2 nanopowder was weighed for the selected concentrations and added to B100 biodiesel. Dispersion was carried out using probe ultrasonication at 20 kHz, 40% amplitude and 300 W for 30 min. A pulse mode of 5 s ON and 2 s OFF was used to limit heat accumulation. The sample container was kept in a water bath during sonication, and the maximum dispersion temperature was maintained at 35 ± 2 °C. Before each tribological test, the prepared nano-enhanced biodiesel was redispersed by 5 min of ultrasonication to restore homogeneity at the contact-supply stage.

Dispersion stability was evaluated using zeta-potential measurements and visual sedimentation observation. The zeta-potential values of the MoS_2 nano-enhanced biodiesel dispersions were -28.6, -30.4, and -31.8 mV for 75, 135 and 150 ppm MoS_2, respectively, indicating moderate-to-good short-term dispersion stability. No visible sedimentation was observed within 24 h after preparation, which was used as the stability time considered for the tribological tests. Slight settling was observed only after prolonged storage at higher MoS_2 concentration; therefore, the conclusions of this study are restricted to freshly prepared or short-term redispersed nano-enhanced biodiesel rather than long-term stored dispersions.

The selected ranges were chosen to represent a practical low-dose nano-additive window and a boundary-lubricated steel contact with increasing severity. The 0-150 ppm range was intended to capture the transition from neat biodiesel to a concentration high enough to form an additive-assisted boundary layer without intentionally testing heavily loaded suspensions. The 10-40 N load range progressively increases asperity contact and contact pressure, while the 0.25-1.00 m/s speed range assesses whether sliding-assisted replenishment and shear of the boundary film improve performance. A 300 s duration was used because the time-dependent COF curves reached a quasi-steady plateau before the end of the test.

A three-factor, three-level Box-Behnken design was used to generate the fifteen experimental conditions listed in Table 4. Each design condition was tested three times, and the reported responses were expressed as mean ± standard deviation for COF, wear rate and post-test average surface roughness (Ra). The resulting data set is provided in Table 5.

Table 4. Box-Behnken experimental matrix for tribological testing

Run	X_1	X_2	X_3	Nano-additive (ppm)	Load (N)	Speed (m/s)
1	-1	-1	0	0	10	0.625
2	+1	-1	0	150	10	0.625
3	-1	+1	0	0	40	0.625
4	+1	+1	0	150	40	0.625
5	-1	0	-1	0	25	0.25
6	+1	0	-1	150	25	0.25
7	-1	0	+1	0	25	1.00
8	+1	0	+1	150	25	1.00
9	0	-1	-1	75	10	0.25
10	0	+1	-1	75	40	0.25
11	0	-1	+1	75	10	1.00
12	0	+1	+1	75	40	1.00
13	0	0	0	75	25	0.625
14	0	0	0	75	25	0.625
15	0	0	0	75	25	0.625

2.3 Statistical modelling

The experimental data were fitted to second-order polynomial models in terms of the coded variables X_1 (nano-additive concentration), X_2 (load), and X_3 (sliding speed). The general model used for each response was:

$$Y = \beta_0 + \beta_1 X_1 + \beta_2 X_2 + \beta_3 X_3 + \beta_{12} X_1 X_2 + \beta_{13} X_1 X_3 + \beta_{23} X_2 X_3 + \beta_{11} {X_1}^2 + \beta_{22} {X_2}^2 + \beta_{33} {X_3}^2 + \varepsilon. \quad (1)$$

where Y is the response of interest and ε is the residual error. Model significance, lack of fit, individual coefficients, predicted-versus-experimental agreement, and confirmation-test errors were used to evaluate model adequacy before optimization.

3. RESULTS AND DISCUSSION

3.1 Experimental response trends

The experimental responses in Table 5 show clear and physically consistent trends. The highest COF occurred at 0 ppm MoS_2, 40 N, and 0.625 m/s (0.132), whereas the lowest measured COF was 0.094 at either 150 ppm and 1.00 m/s or at 75 ppm, 10 N, and 1.00 m/s. This corresponds to a reduction of approximately

28.8% relative to the highest-friction condition. Wear rate decreased from 4.20 x 10^{-6} mm^3/N·m at 0 ppm and 40 N to 2.30 x 10^{-6} mm^3/N·m at 150 ppm and 10 N, representing an approximate 45.2% reduction. Surface roughness followed the same tendency, decreasing from 0.44 to 0.26 μm, which indicates that the improved lubrication condition reduced ploughing and severe asperity damage.

Table 5. Experimental tribological results for the Box-Behnken design.

Run	NA (ppm)	L(N)	V (m/s)	COF ± SD	WR (×10^{-6} mm^3/N·m ± SD)	Ra (μm) ± SD
1	0	10	0.625	0.115 ± 0.003	3.10 ± 0.15	0.32 ± 0.02
2	150	10	0.625	0.098 ± 0.003	2.30 ± 0.12	0.26 ± 0.01
3	0	40	0.625	0.132 ± 0.004	4.20 ± 0.20	0.44 ± 0.02
4	150	40	0.625	0.112 ± 0.004	3.10 ± 0.18	0.34 ± 0.02
5	0	25	0.25	0.128 ± 0.004	4.00 ± 0.22	0.40 ± 0.02
6	150	25	0.25	0.110 ± 0.003	3.00 ± 0.16	0.33 ± 0.02
7	0	25	1.00	0.112 ± 0.003	3.30 ± 0.18	0.34 ± 0.02
8	150	25	1.00	0.094 ± 0.003	2.50 ± 0.14	0.27 ± 0.01
9	75	10	0.25	0.110 ± 0.003	2.90 ± 0.14	0.30 ± 0.01
10	75	40	0.25	0.126 ± 0.004	3.80 ± 0.20	0.41 ± 0.02
11	75	10	1.00	0.094 ± 0.003	2.50 ± 0.13	0.26 ± 0.01
12	75	40	1.00	0.110 ± 0.004	3.00 ± 0.16	0.33 ± 0.02
13	75	25	0.625	0.101 ± 0.003	2.80 ± 0.14	0.29 ± 0.01
14	75	25	0.625	0.103 ± 0.002	2.85 ± 0.12	0.29 ± 0.01
15	75	25	0.625	0.100 ± 0.003	2.75 ± 0.13	0.28 ± 0.01

The trends indicate that MoS_2 concentration, load, and speed did not affect the contact independently. Increasing load promoted asperity penetration, plastic deformation, and abrasive/adhesive interaction, which increased COF, wear rate, and Ra. Increasing MoS_2 concentration reduced direct metallic contact by supplying shearable platelets to the interface and by assisting the formation of a protective layer. Higher sliding speed lowered COF and wear within the tested range, most likely because it improved lubricant entrainment/replenishment and promoted easier shearing of the boundary film. The lower Ra values at high additive concentration and low load are therefore consistent with a smoother wear track formed by reduced ploughing and partial filling of surface valleys by additive-derived and biodiesel-derived surface films.

3.2 Modelling and interpretation of COF

The ANOVA results for COF are presented in Table 6. The model was statistically significant ($p < 0.0001$), while lack of fit was not significant ($p = 0.3321$), indicating that the quadratic model adequately represented the experimental data. The model statistics were satisfactory, with $R^2 = 0.945$, adjusted $R^2 = 0.931$, and predicted $R^2 = 0.906$.

The physical meaning of the regression coefficients is consistent with the measured trends. The negative coefficient of X_1 shows that increasing MoS_2 concentration reduced COF, while the positive coefficient of X_2 shows that increasing load increased COF. The negative coefficient of X_3 indicates that higher sliding speed reduced COF within the tested range. The positive ${X_1}^2$ and ${X_2}^2$ terms reveal curvature, meaning that the response does not change linearly over the entire design space. The weak interaction terms suggest that the COF response was controlled mainly by main effects and curvature rather than by strong two-factor coupling. The fitted coded COF model is:

$$\mathbf{COF} = \mathbf{0.10252} - \mathbf{0.01000X_1} + \mathbf{0.00765X_2} - \mathbf{0.00758X_3} - \mathbf{0.00037X_1X_2} + \mathbf{0.00077X_1X_3} + \mathbf{0.00134X_2X_3} + \mathbf{0.00664}{X_1}^2 + \mathbf{0.00620}{X_2}^2 + \mathbf{0.00108}{X_3}^2. \quad (2)$$

Table 6. ANOVA results for coefficient of friction (COF).

Source	DF	Adj SS	Adj MS	F-value	p-value
Model	9	0.006061	0.000673	66.844	<0.0001
Linear	3	0.005181	0.001727	171.401	<0.0001
X_1 Nano concentration	1	0.002400	0.002400	238.199	<0.0001
X_2 Load	1	0.001403	0.001403	139.281	<0.0001
X_3 Speed	1	0.001378	0.001378	136.724	<0.0001
Interaction	3	0.000030	0.000010	1.005	0.4020
X_1X_2	1	0.000002	0.000002	0.167	0.6857
X_1X_3	1	0.000007	0.000007	0.714	0.4039
X_2X_3	1	0.000022	0.000022	2.135	0.1528
Quadratic	3	0.000928	0.000309	30.701	<0.0001
X_1^2	1	0.000489	0.000489	48.525	<0.0001
X_2^2	1	0.000426	0.000426	42.290	<0.0001
X_3^2	1	0.000013	0.000013	1.287	0.2643
Residual error	35	0.000353	0.000010	—	—
Lack-of-fit	3	0.000035	0.000012	1.182	0.3321
Pure error	32	0.000317	0.000010	—	—
Total	44	0.006414	—	—	—

The Pareto chart in Figure 3 confirms that nano-additive concentration was the dominant factor for COF, followed by load and sliding speed. The residual plots in Figure 4 show approximate normality and no obvious trend with fitted values or run order, supporting the assumptions of the regression model. The contour and surface plots in Figures 5 and 6 show that COF is minimized at high MoS_2 concentration, low-to-moderate load, and high speed. The main-effect and interaction plots in Figures 7 and 8 further confirm that the COF response is governed primarily by additive concentration, load, and speed rather than by strong interaction effects.

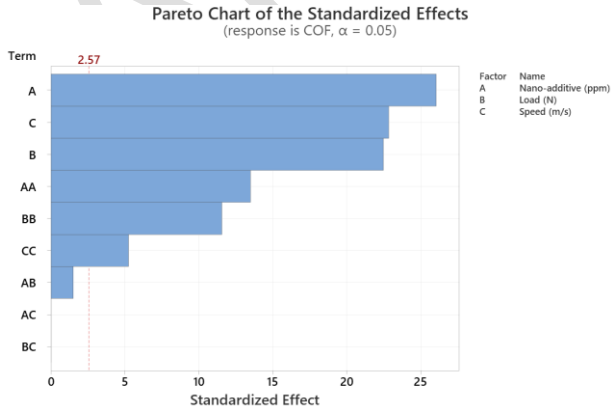

Fig. 3. Pareto chart presenting the standardized effects influencing COF.

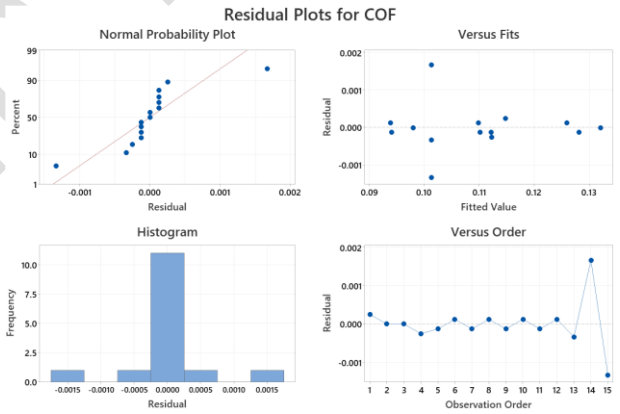

Fig. 4. Residual plots for assessing the validity of the COF regression model.

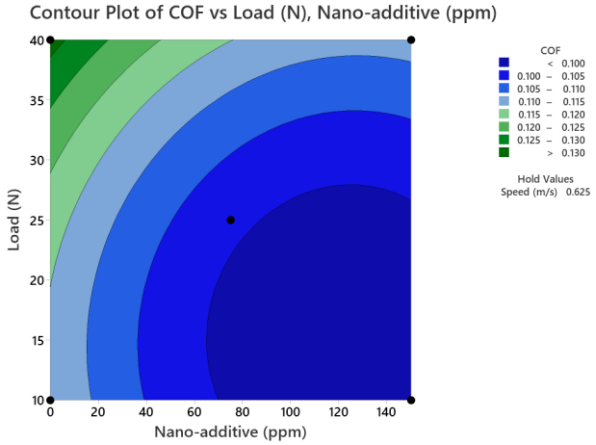

Fig. 5. Contour plot of COF versus load and nano-additive concentration with speed maintained constant.

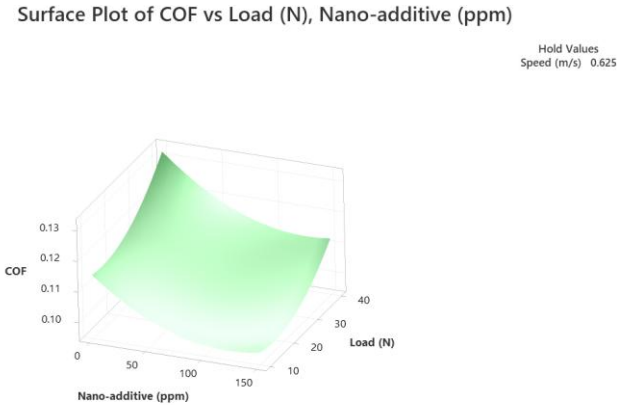

Fig. 6. Surface response plot of COF as influenced by load and nano-additive concentration.

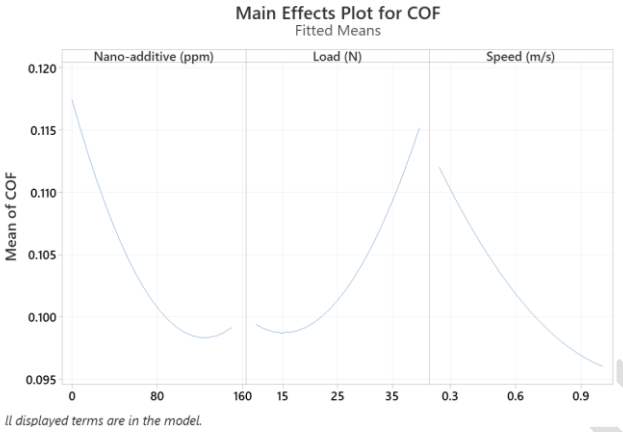

Fig. 7. Main effects plot for COF.

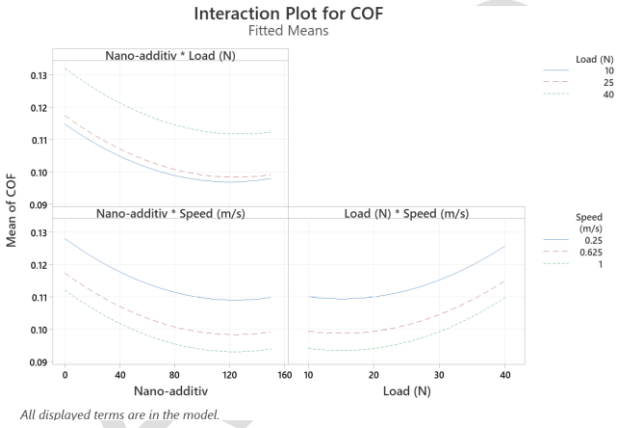

Fig. 8. Interaction effects plot for COF.

3.3 Modelling and interpretation of wear rate

The wear-rate model exhibited adequacy comparable to that of the COF model. Table 7 shows a highly significant model ($p < 0.0001$) with $R^2 = 0.902$, adjusted $R^2 = 0.877$, and predicted $R^2 = 0.831$. The lack-of-fit term was not significant at the 5% level ($p = 0.0697$), confirming that the quadratic model was acceptable for the present data.

For wear rate, the three linear terms were highly significant and the load-speed interaction was also significant ($p = 0.0110$). The negative X_1 coefficient confirms the anti-wear role of MoS_2, while the positive X_2 coefficient shows the damaging effect of increasing load. The negative X_3 coefficient indicates that higher speed reduced wear within the tested range. The significant negative X_2X_3 coefficient suggests that the wear increase caused by load was partly moderated at higher sliding speed, most likely because higher speed improved boundary-film renewal and reduced the residence time of asperity junctions. The fitted coded wear-rate model, with wear rate expressed in 10^{-6} mm^3/N·m, is:

$$WR = 2.82627 - 0.41514X_1 + 0.41209X_2 - 0.29690X_3 - 0.02608X_1X_2 - 0.05668X_1X_3 - 0.14511X_2X_3 + 0.21896{X_1}^2 + 0.09915{X_2}^2 + 0.10188{X_3}^2. \quad (3)$$

The standardized-effects chart in Figure 9 shows that nano-additive concentration, load, and speed were the controlling factors for wear rate. The residual plots in Figure 10 show no severe departure from normality or constant variance. Figures 11 and 12 indicate that wear rate is minimized under low load, high speed, and moderate-to-high MoS_2 concentration. The main-effect and interaction plots in Figures 13 and 14 make the load-speed coupling more evident than in the COF response.

Table 7. ANOVA results for wear rate.

Source	DF	Adj SS	Adj MS	F-value	p-value
Model	9	11.3035	1.2559	35.855	<0.0001
Linear	3	10.3274	3.4425	98.275	<0.0001
X_1 Nano concentration	1	4.1362	4.1362	118.079	<0.0001
X_2 Load	1	4.0756	4.0756	116.349	<0.0001
X_3 Speed	1	2.1156	2.1156	60.395	<0.0001
Interaction	3	0.2994	0.0998	2.849	0.0514
X_1X_2	1	0.0082	0.0082	0.233	0.6323
X_1X_3	1	0.0386	0.0386	1.101	0.3013

X_2X_3	1	0.2527	0.2527	7.214	0.0110
Quadratic	3	0.7550	0.2517	7.184	0.0007
X_1^2	1	0.5311	0.5311	15.161	0.0004
X_2^2	1	0.1089	0.1089	3.108	0.0866
X_3^2	1	0.1150	0.1150	3.282	0.0786
Residual error	35	1.2260	0.0350	—	—
Lack-of-fit	3	0.2398	0.0799	2.593	0.0697
Pure error	32	0.9863	0.0308	—	—
Total	44	12.5295	—	—	—

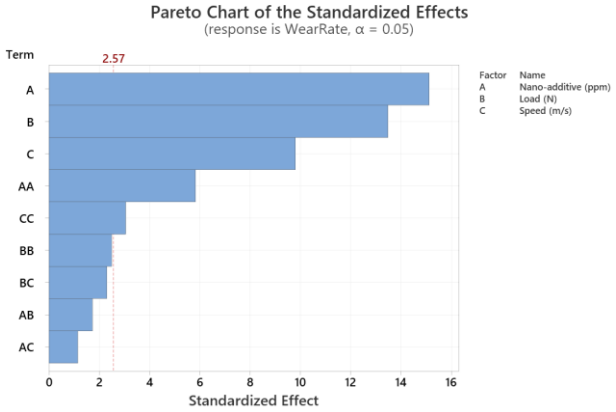

Fig. 9. Pareto chart presenting the standardized effects for wear rate.

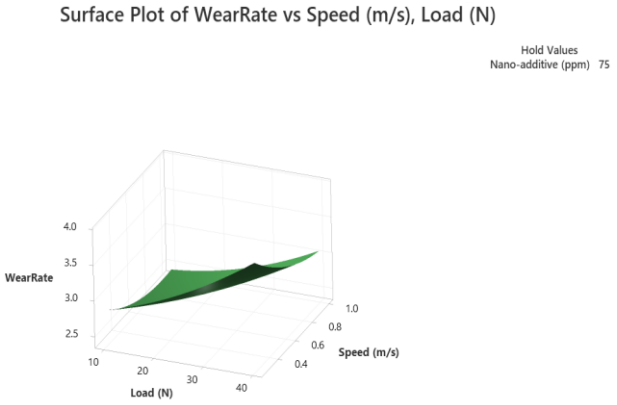

Fig. 12. Surface plot of wear rate as a function of load and speed.

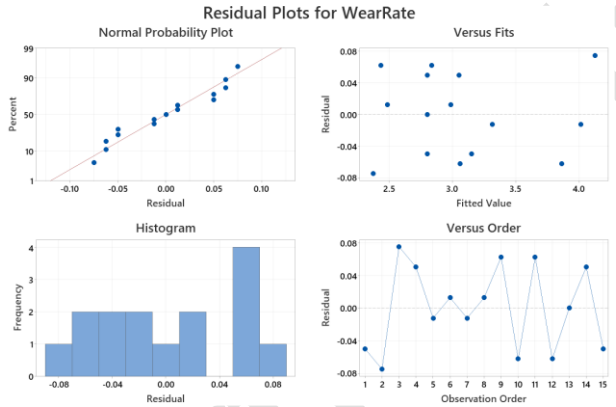

Fig. 10. Residual plots for assessing the validity of the wear regression model.

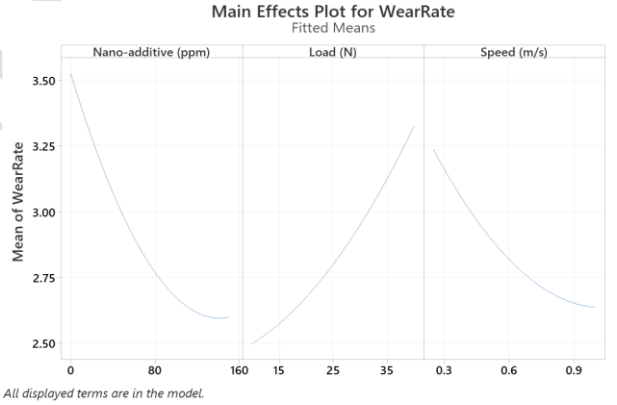

Fig. 13. Main effects plot for wear rate.

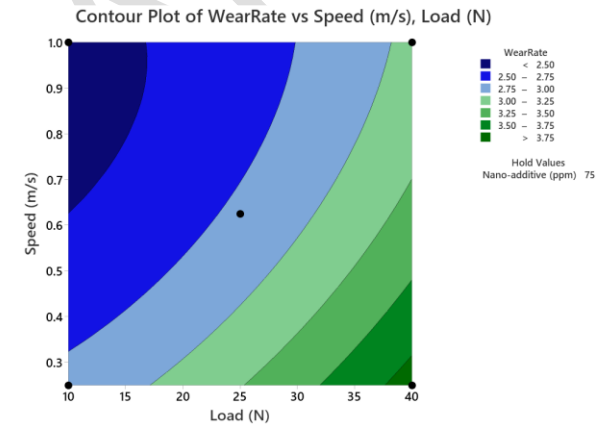

Fig. 11. Contour plot of wear rate as a function of load and speed (nano-additive held constant).

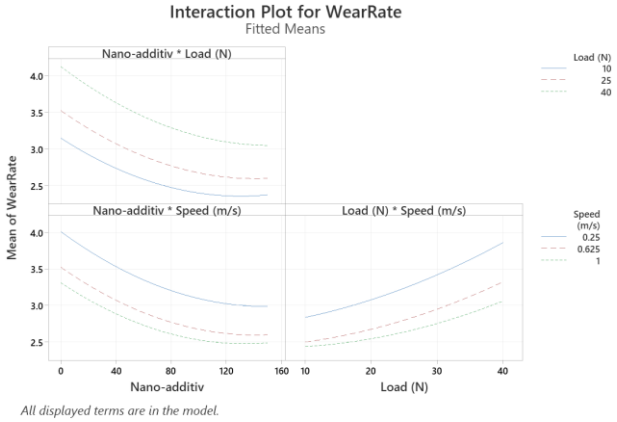

Fig. 14. Interaction effects plot for wear rate.

This behaviour is reasonable because wear depends not only on instantaneous friction but also on repeated asperity fracture, debris generation, and the ability of the lubricant/additive layer to remain active under contact pressure.

The coefficients compiled in Table 8 provide the numerical basis for Equations (2) and (3). For COF, the negative X_1 and X_3 coefficients and the positive X_2 coefficient quantify the friction-reducing effect of MoS_2 and speed and the friction-increasing effect of load, whereas the positive X_1^2 and X_2^2 terms confirm curvature. For wear rate, the same signs of the linear coefficients confirm the anti-wear action of MoS_2 and the damaging effect of load, while the negative X_2X_3 coefficient confirms that higher speed partly moderated load-induced wear.

Table 8. Regression coefficients of the quadratic models.

COF				
Term	**Coefficient**	**Std. Error**	**t-value**	**p-value**
Intercept	0.10252	0.00106	96.897	<0.0001
X_1	-0.01000	0.00065	-15.434	<0.0001
X_2	0.00765	0.00065	11.802	<0.0001
X_3	-0.00758	0.00065	-11.693	<0.0001
X_1X_2	-0.00037	0.00092	-0.408	0.6857
X_1X_3	0.00077	0.00092	0.845	0.4039
X_2X_3	0.00134	0.00092	1.461	0.1528
X_1^2	0.00664	0.00095	6.966	<0.0001
X_2^2	0.00620	0.00095	6.503	<0.0001
X_3^2	0.00108	0.00095	1.135	0.2643
Wear-rate				
Intercept	2.82627	0.06239	45.302	<0.0001
X_1	-0.41514	0.03820	-10.866	<0.0001
X_2	0.41209	0.03820	10.787	<0.0001
X_3	-0.29690	0.03820	-7.771	<0.0001
X_1X_2	-0.02608	0.05403	-0.483	0.6323
X_1X_3	-0.05668	0.05403	-1.049	0.3013
X_2X_3	-0.14511	0.05403	-2.686	0.0110
X_1^2	0.21896	0.05624	3.894	0.0004
X_2^2	0.09915	0.05624	1.763	0.0866
X_3^2	0.10188	0.05624	1.812	0.0786

Figure 15 compares the predicted and experimental values for COF and wear rate. The points lie close to the diagonal trend for both responses, confirming that the models capture the main experimental variation. The agreement is tighter for COF than for wear rate, which is consistent with the higher predicted R^2 of the COF model; however, the wear-rate plot still follows the same trend and is adequate for response optimization within the tested design space.

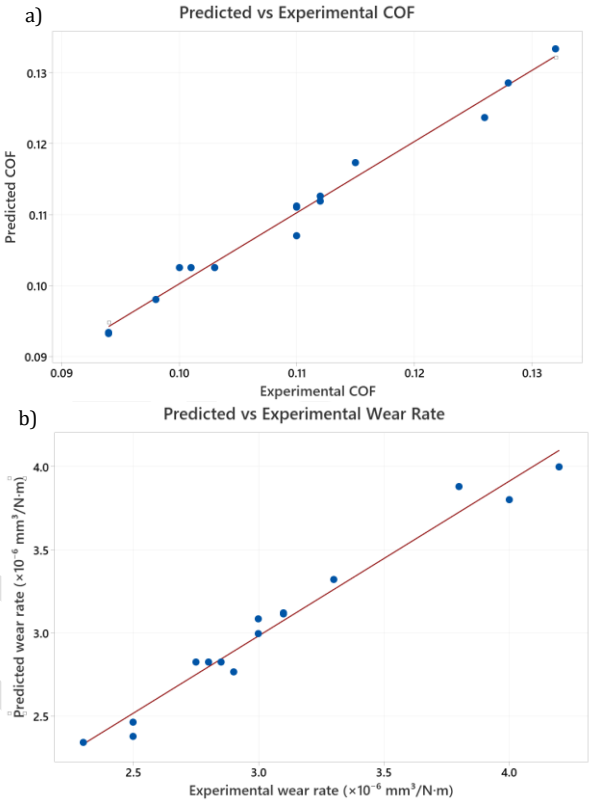

Fig. 15. Predicted versus experimental values for (a) COF and (b) wear rate, showing model validation.

3.4 Optimization and confirmation

The response optimizer in Figure 16 identified the best operating region at high nano-additive concentration, low load and relatively high sliding speed. The exact desirability solution was 125.758 ppm MoS_2, 10 N load and 0.8485 m/s speed, with predicted values of 0.09313 COF and 2.3078 x 10^{-6} mm^3/N·m wear rate. Because this exact condition is inconvenient for routine experimental setting, a nearby practical confirmation point of 135 ppm MoS_2, 12 N and 1.00 m/s was selected. As summarized in Table 9, the model-predicted responses at this confirmation point were 0.090 COF, 2.25 x 10^{-6} mm^3/N·m wear rate and 0.25 µm Ra, while the measured responses were 0.093 ± 0.002, 2.34 ± 0.09 x 10^{-6} mm^3/N·m and 0.26 ± 0.01 µm, respectively. The absolute errors of 3.33-4.00% indicate that the model slightly under-predicted the practical confirmation responses, but the

deviations are within an acceptable range for tribological testing and support the predictive utility of the RSM model.

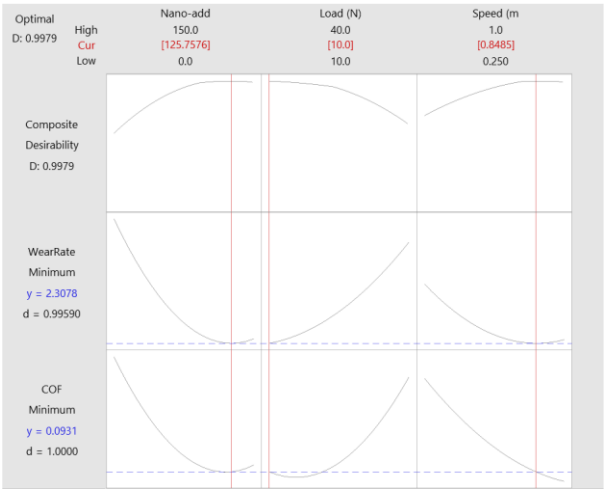

Fig. 16. Multi-response optimization plot using desirability function approach.

Table 9. Optimization results and confirmation test comparison.

Response	Predicted value	Experimental value (mean ± SD)	Absolute error (%)
COF	0.090	0.093 ± 0.002	3.33
Wear rate ($\times 10^{-6}$ $mm^3/N{\cdot}m$)	2.25	2.34 ± 0.09	4.00
Ra after test (μm)	0.25	0.26 ± 0.01	4.00

The time-dependent COF curves in Figure 17 provide an additional performance comparison. The nano-enhanced biodiesel reached the lowest steady-state COF and stabilized faster than neat biodiesel and diesel. The plateau behaviour also supports the use of a 300 s test duration for the present comparative study because friction had reached a quasi-steady state before the end of the test.

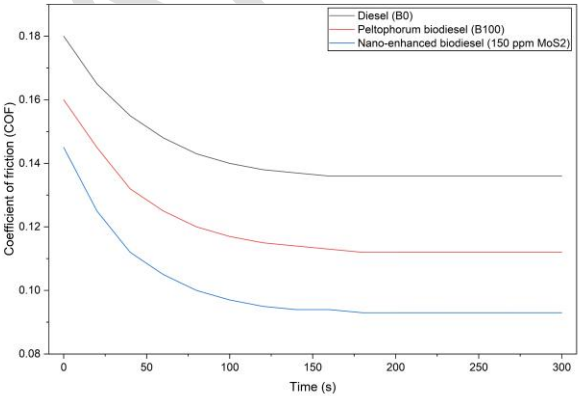

Fig. 17. Variation of coefficient of friction (COF) with time for diesel (B0), Peltophorum biodiesel (B100), and nano-enhanced biodiesel.

3.5 Scanning electron microscope image analysis of MoS_2 nanoparticles

The FESEM images in Figure 18 show the platelet/nanosheet-like morphology of the MoS_2 nano-additive. The particles appear as agglomerated clusters, which is typical for nanoscale MoS_2 because adjacent sheets can attract each other through van der Waals forces. At higher magnification, the lamellar and wrinkled sheet-like arrangement is more visible, supporting the selection of MoS_2 as a shearable solid additive. The interpretation is limited to powder morphology; it does not by itself prove long-term dispersion stability in biodiesel.

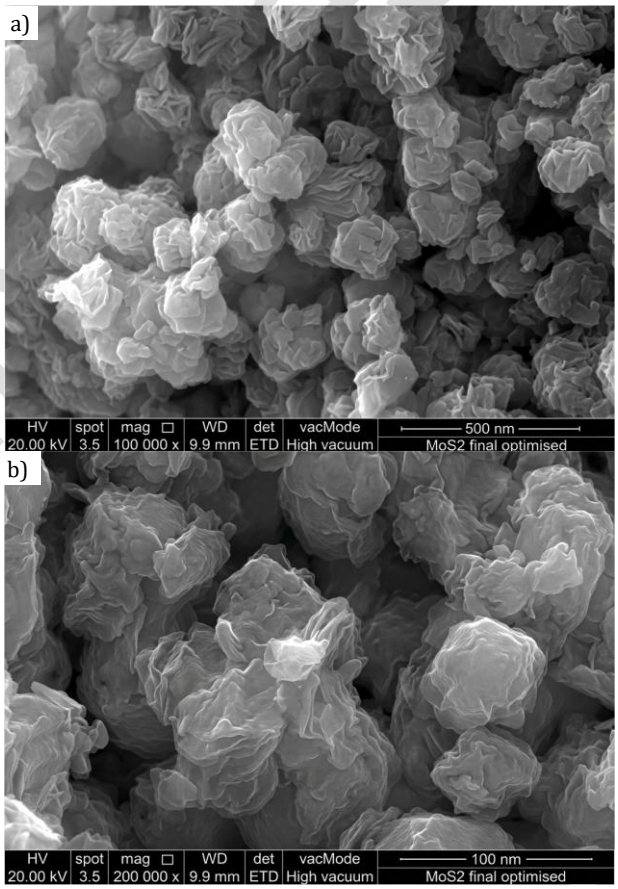

Fig. 18. FESEM micrographs of MoS_2 nanoparticles: (a) 200,000x magnification and (b) 100,000x magnification.

3.6 Surface analysis and lubrication mechanism

The worn surfaces of the AISI 52100 steel discs were characterized using X-ray diffraction (XRD), scanning electron microscopy (SEM), and energy-dispersive spectroscopy (EDS). XRD analysis was carried out using a Rigaku SmartLab X-ray

diffractometer (Rigaku Corporation, Japan) equipped with Cu-Kα radiation. SEM and EDS analyses were performed using a TESCAN MIRA 3 field-emission scanning electron microscope (TESCAN, Czech Republic) equipped with a Bruker Quantax 200 EDS detector (Bruker, Germany).

After completion of the pin-on-disc test, the worn steel disc was carefully removed from the tribometer without touching the wear track. The worn surface was gently rinsed with n-hexane to remove loosely attached biodiesel residue and free wear debris and then dried using warm air at room temperature. No grinding, polishing, or ultrasonic cleaning was performed after the wear test so that the thin tribofilm formed during boundary lubrication could be preserved.

For XRD analysis, the worn disc was mounted directly on the XRD sample holder with the wear track facing upward and positioned at the centre of the incident X-ray beam. The XRD scan was carried out over a 2θ range of 10°-90° using a step size of 0.02° and a scan rate of 2°/min. The operating voltage and current were maintained at 40 kV and 30 mA, respectively. The obtained diffraction peaks were compared with standard reference patterns to identify MoS_2, MoO_3, Fe_3O_4, α-Fe_2O_3 and α-Fe phases.

For SEM analysis, the worn surface was observed at low and high magnifications to examine the overall wear track, grooves, adhered debris, and tribofilm-covered regions. EDS analysis was performed on selected worn regions to determine the elemental composition of the tribofilm and to link the surface chemistry with the measured COF and wear-rate trends.

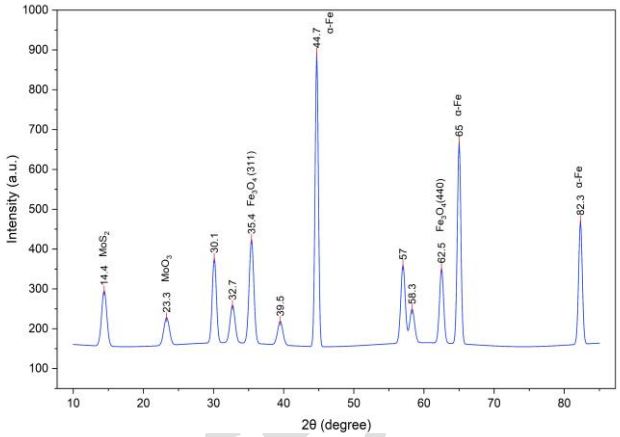

Fig. 19. X-ray diffraction (XRD) pattern of the worn surface lubricated with nano-enhanced biodiesel.

The chemical signatures of the worn surface support the statistical trends, but they should be interpreted as evidence of a thin and heterogeneous tribofilm rather than a thick continuous coating. The XRD pattern in Figure 19 and the phase assignments in Table 10 show weak MoS_2-related peaks, limited MoO_3, iron oxides such as Fe_3O_4 and α-Fe_2O_3, and strong α-Fe peaks from the steel substrate. The strong substrate peaks indicate that the surface layer was thin and/or discontinuous, while the MoS_2 and oxide peaks suggest additive transfer and tribo-oxidation within the wear track.

Table 10. Identified XRD peaks and corresponding phases on worn surfaces.

2θ(°)	intensity	plane	phase	Interpretation
14.4	Weak	(002)	MoS_2	Residual/transfer solid lubricant film
23.3	Very weak	(021)	MoO_3	Limited tribo-oxidation of Mo-containing species
30.1	Medium	(220)	Fe_3O_4 (magnetite)	Oxidative tribofilm on worn steel surface
32.7	Weak	(100)	MoS_2	Additive-derived tribofilm residue
35.4	Medium	(311)/(110)	Fe_3O_4 / α-Fe_2O_3	Overlapping oxide reflections from worn surface
39.5	Weak	(103)	MoS_2 / MoO_3 (possible overlap)	Thin tribofilm-related reflection
44.7	Strong	(110)	α-Fe	Steel substrate
57.0	Medium	(511)	Fe_3O_4	Oxidative reaction product
58.3	Weak	(110)	MoS_2	Additive-derived tribofilm phase
62.5	Medium	(440)/(214)	Fe_3O_4 / α-Fe_2O_3	Mixed iron-oxide contribution
65.0	Strong	(200)	α-Fe	Steel substrate
82.3	Medium	(211)	α-Fe	Steel substrate

SEM micrographs of the worn surface lubricated with MoS_2 nano-enhanced biodiesel under the optimized condition of 135 ppm MoS_2, 12 N and 1.00 m/s are shown in Figure 20(a-d). The low-magnification image shows a comparatively smooth worn surface with shallow grooves along the sliding direction, indicating mild abrasive wear. The smoother regions observed on the wear track suggest the formation of a protective tribofilm during boundary lubrication.

At higher magnification, localized adhered tribofilm patches and debris particles are visible. These patches are attributed to MoS_2/oxide-containing tribofilm formed during sliding. The shallow grooves and the absence of severe delamination indicate that MoS_2 nanoparticles reduced direct metal-to-metal contact and suppressed severe surface damage. The EDS spectrum in Figure 20(e) and the peak assignment in Table 11 confirm the presence of C, O, Mo, S, Fe and Cr on the worn surface. Carbon and oxygen indicate biodiesel-derived organic boundary films and oxidative reaction products, while Mo and S confirm the participation of MoS_2 nanoparticles in tribofilm formation. Fe and Cr are attributed to the AISI 52100 steel substrate.

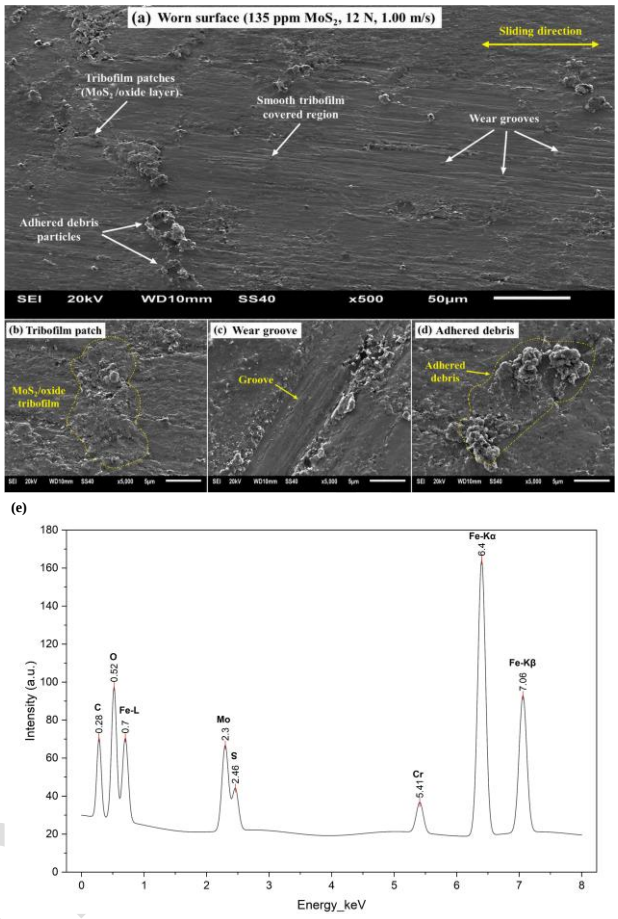

Fig. 20. Worn-surface SEM and EDS.

Table 11. Identified EDS peaks and probable elemental associations on worn surfaces.

Peak position (keV)	Assigned line	Element	Probable origin / interpretation
0.28	Kα	C	Carbonaceous boundary film from biodiesel-derived organic species
0.52	Kα	O	Oxidized wear track; iron oxide / oxidized tribofilm contribution
0.70	Lα	Fe	Exposed steel substrate and/or thin oxide-covered steel
2.29–2.31	Lα / Kα (overlapped)	Mo / S	Additive-derived Mo–S enriched tribofilm; overlap interpreted cautiously
2.46	Kβ	S	Sulfur-containing tribofilm contribution
5.41	Kα	Cr	Minor alloy exposure from AISI 52100 steel
6.40	Kα	Fe	Steel substrate exposure in worn region
7.06	Kβ	Fe	Steel substrate exposure in worn region

Taken together, the experimental responses, roughness values, SEM wear morphology, XRD peaks and EDS elemental signatures support the following lubrication mechanism. MoS_2 platelets enter the contact, align and shear under sliding, and reduce the shear strength of the interface. Simultaneously, biodiesel-derived polar species and iron-oxide reaction products contribute to a heterogeneous composite tribofilm. This film partly fills surface valleys, reduces ploughing, and limits direct metal-to-metal interaction, which explains the simultaneous decrease in COF, wear rate and post-test surface roughness at the optimized condition.

4. CONCLUSION

1. Peltophorum pterocarpum biodiesel satisfied the principal physicochemical limits considered in this study and was therefore a suitable renewable base fluid for evaluating MoS_2 nano-additive enhancement.

2. Within the tested boundary lubrication range, MoS_2 addition reduced COF, wear rate, and post-test surface roughness. The best responses occurred at high additive concentration, low load, and high sliding speed, while increasing load deteriorated all three responses.
3. The quadratic RSM models for COF and wear rate were statistically significant, showed non-significant lack of fit, and gave satisfactory predicted-versus-experimental agreement. The regression coefficients indicate that additive concentration decreases friction/wear, load increases friction/wear, and speed reduces the responses within the tested range.
4. Practical confirmation at 135 ppm MoS_2, 12 N, and 1.00 m/s produced 0.093 ± 0.002 COF, 2.34 ± 0.09 x 10^{-6} $mm^3/N{\cdot}m$ wear rate, and 0.26 ± 0.01 µm roughness, with absolute errors of 3.33-4.00% relative to model predictions.
5. SEM, XRD and EDS results indicate a thin MoS_2-/oxide-/carbon-containing tribofilm on the worn surface. The SEM images show shallow grooves, adhered debris and tribofilm-covered regions, while the XRD and EDS results confirm Mo, S, O, C, Fe and Cr contributions. These findings support a lubrication mechanism involving reduced metal-to-metal contact, low-shear interfacial sliding and partial smoothing/filling of surface asperities. The conclusions apply to freshly prepared or short-term redispersed nano-enhanced biodiesel, as long-term storage stability was not the focus of the present work.

Overall, the study demonstrates the potential of MoS_2-enhanced Peltophorum pterocarpum biodiesel as a sustainable boundary lubricant candidate, provided that dispersion stability and long-duration durability are verified for the intended application.

REFERENCES

[1] D. C. Drown, K. Harper, and E. Frame, "Screening vegetable oil alcohol esters as fuel lubricity enhancers," *Journal of the American Oil Chemists' Society*, vol. 78, no. 6, pp. 579-584, Jun. 2001, doi: 10.1007/s11746-001-0307-y.

[2] D. P. Geller and J. W. Goodrum, "Effects of specific fatty acid methyl esters on diesel fuel lubricity," *Fuel*, vol. 83, no. 17-18, pp. 2351-2356, 2004, doi: 10.1016/j.fuel.2004.06.004.

[3] G. Knothe and K. R. Steidley, "Lubricity of components of biodiesel and petrodiesel: The origin of biodiesel lubricity," *Energy & Fuels*, vol. 19, no. 3, pp. 1192-1200, May 2005, doi: 10.1021/ef049684c.

[4] J. W. Goodrum, D. P. Geller, and T. T. Adams, "Influence of fatty acid methyl esters from hydroxylated vegetable oils on diesel fuel lubricity," *Bioresource Technology*, vol. 96, no. 7, pp. 851-855, 2005, doi: 10.1016/j.biortech.2004.07.006.

[5] M. Muñoz, F. Moreno, C. Monné, J. Morea, and J. Terradillos, "Biodiesel improves lubricity of new low sulphur diesel fuels," *Renewable Energy*, vol. 36, no. 11, pp. 2918-2924, 2011, doi: 10.1016/j.renene.2011.04.007.

[6] F. Sundus, M. A. Fazal, and H. H. Masjuki, "Tribology with biodiesel: A study on enhancing biodiesel stability and its fuel properties," *Renewable and Sustainable Energy Reviews*, vol. 70, pp. 399-412, 2017, doi: 10.1016/j.rser.2016.11.217.

[7] S. H. Hamdan et al., "Influence of fatty acid methyl ester composition on tribological properties of vegetable oils and duck fat derived biodiesel," *Tribology International*, vol. 113, pp. 76-82, 2017, doi: 10.1016/j.triboint.2016.12.008.

[8] N. A. Fathurrahman et al., "Lubricity properties of palm oil biodiesel blends with petroleum diesel and hydrogenated vegetable oil," *Lubricants*, vol. 11, no. 4, Art. no. 176, 2023, doi: 10.3390/lubricants11040176.

[9] M. O. Adeoti, T. Jamiru, T. A. Adegbola, M. Abdullahi, I. Sulaiman, and B. P. Aramide, "Comparative study on lubrication properties of biodiesel and bio-lubricant trans-esterified from desert seed oil with conventional lubricants," *Frontiers in Chemical Engineering*, vol. 6, Art. no. 1451187, 2024, doi: 10.3389/fceng.2024.1451187.

[10] H. Zewdie, G. T. Shunki, D. Syoum, V. Perumal, and P. D. R. Castañeiras, "A review on the impact of bio-additives on tribological behavior of diesel fuels," *Advances in Tribology*, vol. 2024, Art. no. 5530337, 2024, doi: 10.1155/2024/5530337.

[11] L. Razzaq et al., "Effect of additivized biodiesel blends on diesel engine performance, emissions, and lubricity," *Energies*, vol. 13, no. 13, Art. no. 3375, 2020, doi: 10.3390/en13133375.

[12] M. A. Mujtaba et al., "Effect of palm-sesame biodiesel fuels with alcoholic and nanoparticle additives on tribological characteristics of lubricating oil by four ball tribo-tester," *Alexandria Engineering Journal*, vol. 60, no. 5, pp. 4537-4546, 2021, doi: 10.1016/j.aej.2021.03.017.

[13] V. Jokubynienė, S. Slavinskas, and R. Kreivaitis, "The effect of nanoparticle additives on the lubricity of diesel and biodiesel fuels," *Lubricants*, vol. 11, no. 7, Art. no. 290, 2023, doi: 10.3390/lubricants11070290.

[14] Z. Lu et al., "MoS_2 nanomaterials as lubricant additives: A review," *Lubricants*, vol. 11, no. 12, Art. no. 527, 2023, doi: 10.3390/lubricants11120527.

[15] S. B. Mousavi, S. Zeinali Heris, and P. Estellé, "Viscosity, tribological and physicochemical features of ZnO and MoS_2 diesel oil-based nanofluids: An experimental study," *Fuel*, vol. 293, Art. no. 120481, 2021, doi: 10.1016/j.fuel.2021.120481.

[16] X. Zheng et al., "Tribological behavior of Fe_3O_4/MoS_2 nanocomposites additives in aqueous and oil phase media," *Tribology International*, vol. 102, pp. 79-86, 2016, doi: 10.1016/j.triboint.2016.05.024.

[17] Q. Zhang et al., "An efficient lubrication approach to mitigate soot-induced wear: Synergistic repair effect of magnetic MoS_2 composites and magnetic field," *Wear*, vol. 488-489, Art. no. 204182, 2022, doi: 10.1016/j.wear.2021.204182.

[18] T. Nagarajan, N. Sridewi, W. P. Wong, R. Walvekar, and M. Khalid, "Enhanced tribological properties of diesel-based engine oil through synergistic MoS_2-graphene nanohybrid additive," *Scientific Reports*, vol. 13, Art. no. 17424, 2023, doi: 10.1038/s41598-023-43260-1.

[19] C. Zhong, K. Hu, Y. Xu, E. Hu, and X. Hu, "Lubrication antagonism mechanism of nano-MoS_2 and soot particles in ester base oil," *Friction*, vol. 12, pp. 2692-2706, 2024, doi: 10.1007/s40544-024-0904-5.

[20] J. M. Martin et al., "Mechanism of friction reduction of unsaturated fatty acids as additives in diesel fuels," *Friction*, vol. 1, pp. 252-258, 2013, doi: 10.1007/s40544-013-0022-2.

[21] M. I. De Barros Bouchet et al., "Tribochemistry of unsaturated fatty acids as friction modifiers in (bio)diesel fuel," *RSC Advances*, vol. 7, pp. 33120-33130, 2017, doi: 10.1039/C7RA02926H.

[22] S. H. Hamdan et al., "Synergistic nano-tribological interaction between zinc dialkyldithiophosphate (ZDDP) and methyl oleate for biodiesel-fueled engines," *Friction*, vol. 9, pp. 612-626, 2021, doi: 10.1007/s40544-020-0428-4.

[23] M. Freschi et al., "The twelve principles of green tribology: Studies, research, and case studies-A brief anthology," *Lubricants*, vol. 10, no. 6, Art. no. 129, 2022, doi: 10.3390/lubricants10060129.

[24] G. E. P. Box and D. W. Behnken, "Some new three level designs for the study of quantitative variables," *Technometrics*, vol. 2, no. 4, pp. 455-475, 1960, doi: 10.1080/00401706.1960.10489912.

[25] D. C. Montgomery, Design and Analysis of Experiments, 10th ed. Hoboken, NJ, USA: Wiley, 2019.

Nomenclature and Abbreviations Symbols

A - Nano-additive concentration
B - Load
C - Speed
COF - Coefficient of friction
d - Desirability
D - Composite desirability
F - Fisher test value
p - Probability value
R^2 - Coefficient of determination
Adj. R^2 - Adjusted coefficient of determination
Pred. R^2 - Predicted coefficient of determination
NA - Nano-additive
L – Load
V - Sliding speed
R_a - Surface roughness
WR - Wear rate
X_1 - Coded factor for nano-additive concentration
X_2 - Coded factor for load
X_3 - Coded factor for speed
β_0 - Intercept term
$\beta_1, \beta_2, \beta_3$ - Linear regression coefficients
$\beta_{11}, \beta_{22}, \beta_{33}$ - Quadratic regression coefficients
$\beta_{12}, \beta_{13}, \beta_{23}$ - Interaction regression coefficients
y - Predicted response

Units

kV - kilovolt
m/s - metre per second
N - newton
nm - nanometre
ppm - parts per million
s - second
µm - Micrometre

Abbreviations

AISI - American Iron and Steel Institute
ANOVA - Analysis of variance
ASTM - ASTM International
B100 - Neat biodiesel
BBD - Box-Behnken design
COF - Coefficient of friction
DOE - Design of experiments
EDS - Energy dispersive spectroscopy
EN - European Standard
FAME - Fatty acid methyl ester
FESEM - Field emission scanning electron microscopy
MoO_3 - Molybdenum trioxide
MoS_2 - Molybdenum disulfide
RSM - Response surface methodology
SEM - Scanning electron microscopy
XRD - X-ray diffraction